Materials & Design 219 (2022) 110808

Contents lists available at ScienceDirect

Materials & Design

journal homepage: www.elsevier.com/locate/matdes

Changes in the nanoscale asphaltene particles and relaxation spectra of asphalt binders during aging and rejuvenation

Fangjin Li [a], Yuhong Wang [a,*], Miomir Miljković [b], Kin Ming Chan [a]

[a] Department of Civil and Environmental Engineering, The Hong Kong Polytechnic University, Hong Kong, China
[b] Faculty of Civil Engineering and Architecture, University of Niš, Niš, Serbia

HIGHLIGHTS

- Dynamic shear test helps decipher nanoscale changes in asphalt binder during aging and rejuvenation.
- Relaxation spectrum well captures the physicochemical property variations of asphalt binder.
- Increases in asphaltene content, size, and aspect ratio prolong the relaxation process of asphalt binder.
- The equivalent asphaltene particle size (a_{eq}) is proposed to understand nanoscale changes in asphalt binder.

GRAPHICAL ABSTRACT

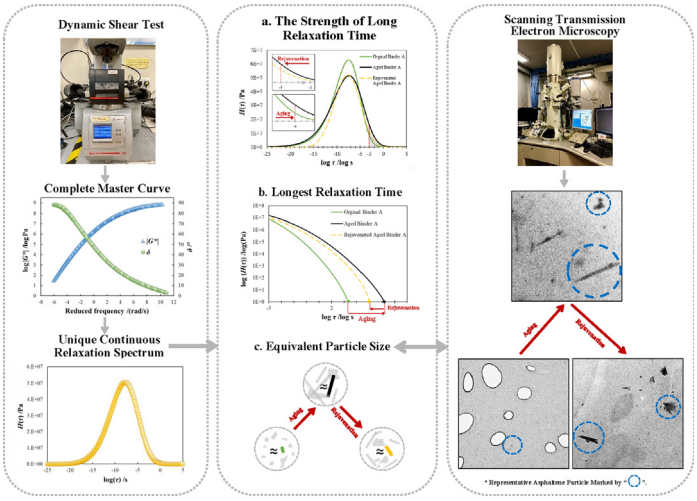

ARTICLE INFO

Article history:
Received 30 December 2021
Revised 6 May 2022
Accepted 30 May 2022
Available online 2 June 2022

Keywords:
Nanoscale asphaltene particles
Relaxation spectra
Aging
Rejuvenation

ABSTRACT

Asphalt binder is a widely used engineering material. It is essentially a nanomaterial with colloidal particles suspended in an oily medium. As asphalt binder ages, the colloidal particles are subject to fundamental physicochemical changes such as agglomeration, which is translated into dramatic engineering property changes of the asphalt binder. In engineering practices, organic rejuvenators are often added to the aged asphalt binder, with the hope of breaking down the nanoparticles and restoring its original engineering properties. However, how the nanoparticles evolve during the aging and rejuvenation of asphalt binder remains hypothetical. This study revealed the fundamental changes of the colloidal particles in asphalt binder during aging and rejuvenation. Moreover, changes in the morphology of colloidal particles are connected to the relaxation spectrum of the asphalt binder. As a result, practitioners do not have to rely on complicated methods and equipment to observe asphalt binders at the microscopic level. Instead, they can employ commonly used engineering tests with a dynamic shear rheometer (DSR) to decipher what occurs at the nanoscale during asphalt binder aging and rejuvenation. This would greatly assist practitioners in material selection and design.

* Corresponding author.
E-mail address: yuhong.wang@polyu.edu.hk (Y. Wang).

https://doi.org/10.1016/j.matdes.2022.110808
0264-1275/

1. Introduction

Asphalt binder, also known as bitumen, is a material widely used in various applications, including paving, waterproofing, and roofing. In chemical characterization, fraction analysis is often conducted to separate the components of asphalt binder into four fractions – saturates, naphthene aromatics (NA or aromatics), polar aromatics (PA or resins), and asphaltenes [1–3]. Of these fractions, asphaltenes and some resins attached to them are the nanoscale solid phase, which is suspended in a fluid medium made of the rest fractions collectively called maltenes. Together, these four fractions form a stable colloidal system [4–7].

A fundamental process that drives the property changes of the asphalt binder is aging. While a small extent of aging beneficially improves the stiffness of asphalt binder, severe aging detrimentally affects its long-term durability. As asphalt binder ages, some NA changes into PA, and some PA changes into asphaltenes, resulting in a net increase of asphaltene content [8]. For a same type of asphalt binder, rheological property changes are well related to changes in asphaltene content [6,9,10]. For different types of asphalt binder, however, relationships between the rheological properties and asphaltene content vary greatly. This is partly due to property variations of maltenes. According to well-established colloidal theories, the properties of a colloidal system are imparted by the content and characteristics of colloidal particles as well as the properties of maltenes [11]. If the maltene viscosity and asphaltene content are known, the viscosities of asphalt binders from different crude oil sources can be very well predicted [6,9,10].

However, some engineering properties of asphalt binders, such as brittleness, fracture, and fatigue, are hard to be predicted through asphaltene content and maltene [9,10]. The properties (e.g., toughness) and morphology (e.g., size, shape) of nanoscale asphaltenes likely play a critical role in determining such properties, but little is known about the true state of asphaltenes in asphalt binder until recently. Assisted with scanning transmission electron microscopy (STEM) and atomic force microscopy (AFM), researchers recently discovered different asphaltene microstructures in asphalt binders [9]. Some asphaltene microstructures are found to be much bigger (hundreds of nanometers or even greater than 1 μm in the longest direction) than those reported in existing literature concerning asphaltenes in petroleum oil (a few nanometers) [12,13], and rod-like crystalline asphaltene microstructures are observed [9,14]. Those asphaltene microstructures were found to be weak and brittle [9]. The unique morphology and brittleness of asphaltene microstructures may explain many property variations of asphalt binders, in addition to asphaltene content and maltene viscosity. Apart from changes in fractions, asphalt binder aging also causes changes in the molecular/microstructural size of the fractions [15,16]. Recent studies on STEM images suggest that aging is associated with increases in the size and the aspect ratio of the asphaltene microstructures [17].

While directly observing asphaltenes in asphalt binders provides useful insights, it is difficult to quantify the effects of asphaltene morphologies on binder properties. Moreover, it is costly and inconvenient to prepare STEM samples and make direct observations, making it impossible to be applied to engineering practices. One alternative approach is to indirectly evaluate the morphological effect of asphaltenes through deciphering asphalt binder properties that are sensitive to asphaltene morphology. Although the viscosity of asphalt binder is theoretically affected by both asphaltene content and morphology, experiments indicate that asphaltene content alone is the predominant factor [9]. Conversely, the relaxation time of the asphalt binder can potentially serve as an indicator of asphaltene morphology because relaxation time is very sensitive to particle morphology in a colloidal system. For instance, the characteristic relaxation time τ_α of a hard spherical colloid with the size of a_0 (radius) in a dilute solution is depicted by Eq. (1) [11], and the characteristic rotational relaxation time τ_r of a rod-like colloidal particle is depicted by Eqs. (2)–(3) [18].

$$\tau_\alpha = \frac{6\pi\eta_s a_0^3}{kT} \tag{1}$$

where τ_α is the characteristic relaxation time of the colloidal particle, η_s is the viscosity of the solution, a_0 is the radius of the colloidal particle, k is the Boltzmann constant (1.38×10^{-23} J/K), and T is the absolute temperature.

$$\tau_r \approx \frac{1}{D_{r0}} \tag{2}$$

$$D_{r0} = \frac{kTln\left(\frac{2L}{d}\right)}{3\pi\eta_s L^3} \tag{3}$$

where τ_r is the characteristic rotational relaxation time of the rod-like colloidal particle, D_{r0} is the rotatory diffusion coefficient, η_s is the solution viscosity, L and d are the length and diameter of the particle, respectively.

As shown in Eqs. (1)–(3), the characteristic relaxation time of the colloidal particles is sensitive to particle size and shape, thereby affecting not only the characteristic relaxation time of a dilute colloid system but also a semi-dilute or concentrated one. Characteristic relaxation time is well related to the longest relaxation time of a colloidal system [19]. Therefore, by examining the relaxation time of the asphalt binder, one may be able to evaluate the size effect of asphaltenes.

After an asphalt binder is aged, a rejuvenator is sometimes added to improve its properties. Rejuvenator often brings noticeable changes in the shear modulus or the viscosity of the rejuvenated asphalt binder [6,20]. This is quite expectable as the rejuvenating agent helps dilute asphaltene content and perhaps also reduces the viscosity of the maltenes. However, the effect of rejuvenation on changes in the size and shape of asphaltene particles remains unknown. Ideally, true rejuvenation should be able to totally dissolve those associated asphaltene microstructures to avoid their negative impacts on the critical engineering properties of the aged asphalt binders. However, there is a paucity of literature on changes in asphaltene microstructures after rejuvenation. This study aims to (1) analyze changes in the relaxation spectra of asphalt binders after aging and rejuvenation, (2) examine asphaltene particle changes in aging and rejuvenation, and (3) establish the connections between changes in relaxation spectra and variations in maltene viscosity and asphaltene particle size. This study evaluated images of observable asphaltene particles in asphalt binders of various aging states and after rejuvenation. Such images provide direct evidence on changes in the asphaltene size and shape after the aging and rejuvenation process and help cross-check the relaxation spectra. In addition, a meticulous effort was made to ensure the reliability of the relaxation spectra: Not only the samples were tested over a wide range of temperature from −34 °C to 130 °C, but a newly developed method was also used to create relaxation spectra to ensure that the consistency of relaxation spectra derived from storage moduli and loss moduli.

2. Materials and methods

2.1. Asphalt binders, rejuvenators, and rejuvenated asphalt binders

Two groups of asphalt binders were used for study. The first group consists of two virgin asphalt binders: One is from the Middle East with a penetration grade of 60/70, high-temperature performance grade of 64, 47.8 °C of softening point, and 225 Pa·s of viscosity at 60 °C; The other one is from Ta He, China with a penetration grade 80/100, high-temperature performance grade of 64,

45.0 °C of softening point, and 160 Pa·s of viscosity at 60 °C. The virgin binders were subjected to short- and long-term aging treatments. The short-term aging was simulated using a rolling thin film oven (RTFO) according to ASTM D2872, while the long-term aging was simulated using one and three cycles of pressure aging vessel (PAV) treatment according to ASTM D6521 for 20 and 60 hr, respectively. The second group consists of extracted and recovered binders from two different in-service roads, where the pavements have been placed for 5 and 10 years, respectively. Resurfacing operations may have occurred on the roads, but the base course has never been replaced. Therefore, the base course was chosen to obtain field-aged binders. The original penetration grade of the binders in these pavements was 60/70, and the binders were provided by the same supplier. Binder extraction and recovery were carried out according to ASTM D2172/D2172M-11 and EN 12697-3.

Corn oil and commercial oil were selected as rejuvenating agents to evaluate changes in the aged asphalt binders after rejuvenation. The corn oil, composed of various fatty acids, is a regular cooking oil, while the commercial oil is a proprietary product specially designed for asphalt recycling.

Four aged asphalt binders, including the two virgin ones after 60 hr of PAV treatments and the two recycled ones, were subjected to rejuvenation treatment. Rejuvenation was done by heating 30 g of each binder in the oven at the temperature of 110 °C for 30 min, and subsequently evenly mixing the binder with a rejuvenator in a 50-ml beaker at 160 °C for 20 min using an overhead rotating mixer with a four-blade propeller stirrer. The rotational speed of the stirrer was set at 250 min^{-1}. Following the earlier experience of having satisfactory workability with the mass fraction of rejuvenator in the range from 3 to 9 % [21], the mass fraction of rejuvenator was fixed at 4.5 % in this research. Note that among the laboratory-aged binders, those treated with PAV for 60 hr were more comparable with field-aged binders in terms of asphaltene content and microstructure morphology. Therefore, they were selected for rejuvenation treatment and subsequent analysis.

In the following discussions, the four different aging levels of base binders were referred to as the penetration grade plus aging level (e.g., 6070Virgin, 6070RTFO, 6070PAV1, 6070PAV3). The field-aged binders were designated as FA plus service years (e.g., FA5 and FA10). The rejuvenated binders in figures or tables were simply represented by "designation of aged sample + rejuvenating agent" (e.g., 80100PAV3 + Commercial oil).

2.2. Physicochemical characterization

A scanning transmission electron microscope (STEM) was used to examine asphaltene microstructures in asphalt binders, including those non-aged, aged, and rejuvenated. The working voltage of the STEM was 200 kV. A thin film of the asphalt specimen was created without solvent casting. This ensures that microstructures in asphalt binders are not affected by solvent during the preparation of STEM samples. Cu 200 mesh grid attached with a holey carbon film was adopted to support the asphalt binder specimen.

Asphaltene fractions in asphalt binders were determined in accordance with the standard ASTM D4124-11. About 3 g of the specimen was used for each asphalt binder. Iso-octane was used to separate the asphaltene fractions, and the maltene fraction was not further separated. After the mass of asphaltenes was determined, the fractions of maltenes were calculated by subtraction.

The rheological properties of asphalt binders, rejuvenators, and maltenes were determined by using a dynamic shear rheometer (DSR). For rejuvenators and maltenes, rotational viscosity was measured using a 50-mm cone-and-plate geometry. The testing condition was set from 20 °C to 140 °C at the shear rates evenly distributed between 0.1 and 400 s^{-1} at the logarithm scale. The viscosities of blended rejuvenators and maltenes were calculated based on the Refutas blending equation by following the ASTM D7152 [22]. For asphalt binders, a small amplitude oscillatory shear (SAOS) test was conducted to ensure that the tests were in the linear viscoelastic range. The test was performed on the binders in a strain-controlled mode at 24 angular frequencies (logarithmically distributed within the range evenly from 0.1 to 30 rad/s) at each temperature, maximally ranging from −34 °C to 130 °C. The DSR setup geometries and the corresponding test temperature for SAOS test are given in Table 1. Note that the actual lowest temperature varied slightly between samples due to the limiting cooling capacity of the DSR equipment, and the actual highest temperature also varied, dependent on the stiffness of the binders. Cautions were taken in the test to ensure that there was no flowing binder at the highest testing temperature (otherwise, it would be discarded) and no slippery issue between the binder and plates at the low testing temperature. All specimens were measured in triplicates. The material's response was quantified by the complex shear modulus $|G^*|$ and phase angle δ. The applied wide range of testing conditions (temperatures and frequencies) enabled the acquisition of the complete rheological response of the binders with phase angle ranging between about 0° and 90°. The purpose of choosing the wide temperature range is to obtain sufficient data for complete relaxation spectra and derive certain rheological properties (e.g., glassy modulus).

2.3. Development and partial validation of the continuous relaxation spectra

2.3.1. Development of the relaxation spectra

A procedure recently proposed was used to develop the continuous relaxation spectra $H(\tau)$ using storage modulus $G'(\omega)$ and loss modulus $G''(\omega)$ obtained from the DSR tests [23]. The details of the procedure and validation of the method refer to Chan and Wang's work [23]. For the interest of completeness, the procedure of developing the relaxation spectrum is briefly introduced as follows.

The continuous relaxation spectrum $H(\tau)$ of an asphalt binder is related to its storage modulus and loss modulus obtained from the dynamic test through the following equations [24]:

$$G'(\omega) = \int_{\tau=\infty}^{\tau=0} H(\tau) \frac{\omega^2\tau^2}{1+\omega^2\tau^2} \cdot d\ln\tau \tag{4}$$

$$G''(\omega) = \int_{\tau=\infty}^{\tau=0} H(\tau) \frac{\omega\tau}{1+\omega^2\tau^2} \cdot d\ln\tau \tag{5}$$

where $G'(\omega)$ is the storage modulus, $G''(\omega)$ is loss modulus, ω is the test frequency, and τ is the relaxation time.

Due to the ill-posedness of the problem, it is difficult to solve the Eqs. (4)–(5) to obtain $H(\tau)$ [25]. Many methods have been proposed for such purpose, and either the storage modulus or loss modulus was used to derive $H(\tau)$. However, results of $H(\tau)$ obtained from the storage modulus often mismatch the ones

Table 1
DSR setup geometries and the corresponding test temperatures for the SAOS tests (Note that the actual lowest temperature dependent on the cooling capacity of the DSR, and the actual highest temperature dependent on the stiffness of the binder).

DSR plate diameter (mm)	DSR gap size (mm)	Test temperature (°C)
25	1	50 to 130 with the increment of 10
8	2	−8, −4, 0, 10, 20, 30, 40, 50
4	2	−34, −32, −30, −28, −26, −24, −22, −20, −16, −12, −8

obtained from the loss modulus. In a previous study, the authors took advantage of the intrinsic relationships of the rheological parameters and developed a simple and robust procedure to derive relaxation spectrum [23].

Firstly, the master curves of the complex shear modulus and phase angle are built from the experimental data using the time temperature superposition (TTS) principle based on the Williams–Landel–Ferry (WLF) equation (Eq. (6)) [26]. The master curve is characterized by the generalized logistic sigmoidal (GLS) model (Eq. (7)) [27]:

$$\log a_T = \frac{-C_1(T-T_r)}{C_2+(T-T_r)} \tag{6}$$

where a_T is the shift factor, T_r is reference temperature of 25 °C, and C_1 and C_2 are fitting parameters.

$$\log|G^*(\omega_r)| = \nu + \frac{\alpha}{\left(1+\lambda e^{\beta+\gamma(\log\omega_r)}\right)^{\frac{1}{\lambda}}}, \omega_r = \alpha_T\omega \tag{7}$$

where ω_r is reduced angular frequency, ω is angular frequency, ν is the equilibrium shear modulus (the lowest possible value of $|G^*|$ obtained for $\omega_r \to 0$, $\nu+\alpha$ is the highest possible value of $|G^*|$ obtained for$\omega_r \to \infty$, and β, γ, and λ are the shape parameters of the sigmoidal function.

Secondly, the phase angle model $\delta(\omega)$ can be obtained from the complex shear modulus based on Kramers-Kronig (KK) relationship (Eq. (8)) and Fuoss-Kirkwood (FK) approximation (Eq. (9)), respectively [28–30].

$$\ln|G^*(\omega)| = -\frac{\omega}{\pi}\int_{\ln u=-\infty}^{\ln u=\infty} \frac{d\left(\left(\delta(u)-\frac{\pi}{2}\right)/u\right)}{d\ln u} \ln\left|\frac{u+\omega}{u-\omega}\right| d\ln u \tag{8}$$

$$\delta(\omega) \approx \frac{\pi}{2}\frac{d\ln|G^*(\omega)|}{d\ln\omega} \tag{9}$$

Thirdly, the relationship between the relaxation spectrum and storage modulus or loss modulus can be expressed by the first-order FK approximation [31]:

$$H(\omega^{-1}) \approx \frac{dG'(\omega)}{d\ln\omega} \tag{10}$$

$$H(\omega^{-1}) \approx \frac{2}{\pi}G''(\omega) \tag{11}$$

Note that the parameters that define the WLF equation and the GLS model are identified through the optimization of the following function. The parameters are subsequently used to derive $H(\tau)$ from $G'(\omega)$ or $G''(\omega)$:

$$\min_{\arg}\left(w_1E_{G^*}+w_2E_\delta+w_3E_H\right) \tag{12}$$

where E_{G^*}, E_δ are the average squared relative errors from the data of $|G^*(\omega)|$, $\delta(\omega)$ and their corresponding values in the prediction models, E_H is the average squared relative differences of $H(\tau)$ obtained from $G'(\omega)$ and $G''(\omega)$, $w_1,\cdots,w_3$ are the weights of the respective errors with the normalizing constrains: $0 \le w_1,\cdots,w_3 \le 1$ and $w_1+\cdots+w_3=1$.

Since the long relaxation time of asphalt binders is very sensitive to the size and morphology of asphaltene particles, relaxation spectra obtained by other methods are expected to generate similar findings.

2.3.2. Partial validation of the relaxation spectra

Although the creep test was not conducted in this study, the completeness of relaxation spectra was validated by comparing the area enclosed by the relaxation spectrum curve and the glassy modulus obtained from test data. The relationship between the relaxation modulus $G(t)$ and relaxation spectrum is shown in Eq. (13).

$$G(t) = \int_{-\infty}^{\infty} H(\tau)e^{-\frac{t}{\tau}}d(\ln\tau) \tag{13}$$

where t is time, and τ is the relaxation time.

By setting t = 0, Eq. (13) becomes:

$$G(t=0) = \int_{-\infty}^{\infty} H(\tau)d(\ln\tau) \tag{14}$$

where $G(t=0)$ represents the instantaneous shear modulus as relaxation starts. It is equal to the integrated area under the function of $H(\tau)$.

In an oscillation shear test, the glassy modulus G_g is defined as the upper limiting modulus of binder samples at low temperatures and high frequencies or short loading times [32]. A regression curve of logarithm complex shear modulus versus phase angle can be developed to estimate glassy modulus at very small phase angles. The intercept of the regression curve, i.e, when phase angle = 0°, is the glassy modulus [32]. The value of G_g should be theoretically equal to $G(t=0)$. Taking the 60/70 non-aged binder as an example, the curve between $\log G^*$ and δ at −28 °C is shown in Fig. 1. The minimum phase angle obtained from the experimental test is around 2°. Given that the R^2 is greater than 0.90, $\log|G^*|$ can be confidently estimated from phase angle, which is about 0.97 GPa. $|G^*|$ obtained from the oscillation shear test was subsequently used to crosscheck the integrated area under the function of $H(\tau)$.

2.4. Interpretation of the continuous relaxation spectra

2.4.1. Relaxation strength at long relaxation time

As shown in Eqs. (1)–(3), relaxation time is sensitive to the size and shape of colloidal particles. Larger molecules or microstructures correspond to longer relaxation time and vice versa. In a previous study, the relaxation spectrum of the asphalt binder was equally divided into 13 slices over the log scale of the relaxation time range. The proportion of the right five slices (from the 9th to 13th slice) were used to represent the relaxation spectrum for large microstructures [33]. This method, however, is affected by the range of $\log(\tau)$ and the overall distribution of $H(\tau)$. To make the interpretation more consistent, this study chose the logarithmic relaxation time of −3 as the cut-off point (Eq. (15), Fig. 2).

$$I_{H,\ LMS} = \int_{-3}^{+\infty} H(\tau)d(\ln\tau) \tag{15}$$

where $I_{H,\ LMS}$ is the portion of the relaxation spectrum that corresponds to the effect arising from large molecules or microstructures.

2.4.2. The longest relaxation time and equivalent colloidal size

The longest relaxation time can also be obtained from the relaxation spectrum, as shown in Fig. 3. In a non-diluted colloidal system with spherical particles, the longest relaxation time τ_w is related to the characteristic relaxation time τ_p, given by:

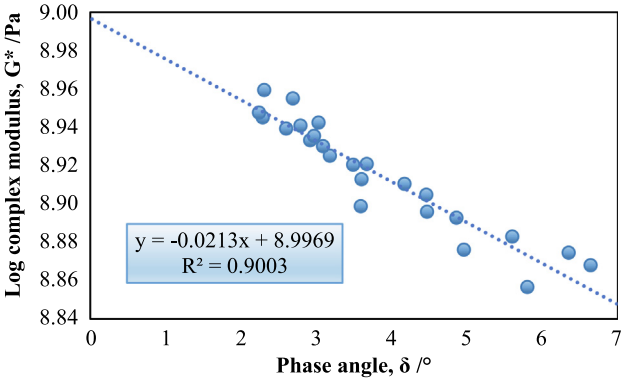

Fig. 1. Relationship between log G^* and δ of the 60/70 non-aged binder.

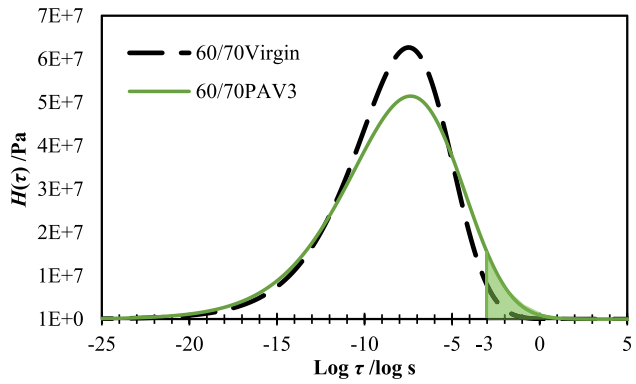

Fig. 2. The relaxation spectra of asphalt binder 60/70 at two aging states (Reference temperature: 25 °C). Note that log(τ) = −3 was chosen as the cut-off point because it was close to the inflection points of most relaxation spectra, but the selection of a cut-off point between −3 and 2 did not largely affect the interpretation results.

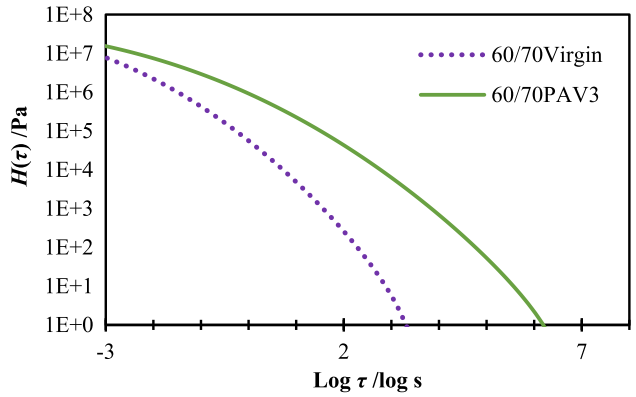

Fig. 3. The longest relaxation time of asphalt binder 60/70 at two aging states (Note: Unlike Fig. 2, the y-axis ($H(\tau)$) is presented in a logarithm scale).

$$\tau_w \approx 0.5\tau_p \tag{16}$$

where τ_w is the longest relaxation time of the non-diluted colloidal system (at least for the volume fraction of the particle phase less than 0.5 [19]), and τ_p is the characteristic relaxation time of the system. The characteristic relaxation time is calculated by the following equation:

$$\tau_p \approx \frac{\pi\eta_\infty' a^3}{kT} \tag{17}$$

where η_∞' is the limiting high–frequency viscosity, which is a function of the viscosity of the medium and the volume fraction of the particles, and a is the particles radius. Note that η_∞' replaces η_s in Eq. (1) and Eq. (3).

η_∞' is difficult to be measured. Assuming that the suspension medium is a viscous fluid with viscosity independent of shear rate, one can write:

$$\eta_{r,\infty}' = \frac{\eta_\infty'}{\eta_s} \tag{18}$$

where $\eta_{r,\infty}'$ is the limiting high–frequency relative viscosity and η_s is the viscosity of the suspension medium (solution).

Several equations have been developed to estimate $\eta_{r,\infty}'$ based on the volume fraction of the particles. Three examples are shown in Eq. (19) [33], Eq. (20) [34], and Eq. (21) [35]. Note that Eq. (21) applies to deionized suspensions [11].

$$\eta_{r,\infty}' = \left(1 - \frac{\phi}{\phi_{max}}\right)^{-[\eta]\times\phi_{max}} \tag{19}$$

where ϕ is the volume concentration of the particle, ϕ_{max} is the maximum packing volume concentration, and $[\eta]$ = 2.5 is the intrinsic viscosity.

$$\eta_{r,\infty}' = \frac{1+1.5\phi\left(1+\phi-0.189\phi^2\right)}{1-\phi\left(1+\phi-0.189\phi^2\right)}, 0 \le \phi < 0.64 \tag{20}$$

$$\eta_{r,\infty}' = 1 + 2.5\phi(1+\phi) + 7.9\phi^3 \tag{21}$$

The maximum packing volume concentration ϕ_{max} varies in literature, ranging from about 0.638 to nearly 0.74 for nearly spherical particles [11]. Using Eqs. (19)–(21), changes of high-frequency viscosity with volume fraction are compared and shown in Fig. 4. As shown in the figure, results from the different equations and assumptions are close, especially at the low volume fraction.

Because the longest relaxation time can be obtained from the relaxation spectrum, Eq. (17) is proposed in this study to calculate the "equivalent" size of asphaltene particles (Eq. (22)). Such "equivalent" size considers the overall effect of the heterogeneous asphaltene particles that vary in size and shape, as well as the complex interactions between the particles.

$$a_{eq} \approx \left(\frac{kT\tau_p}{\pi\eta_\infty'}\right)^{1/3} \tag{22}$$

where a_{eq} is the equivalent particle size, η_∞' is calculated using Eq. (20) and Eq. (18), and all the other parameters are the same as those in Eq. (17).

3. Results and discussion

3.1. Basic properties

The rotational viscosities of two rejuvenators at different temperatures are shown in Fig. 5. For comparison purposes, the viscosity of maltenes extracted from 6070PAV3 is also exhibited in the figure. The maltenes were obtained by firstly separating maltenes from asphaltenes based on the standard fraction analysis procedure (ASTM D4121-09), except that maltenes were not further separated into saturates, NA (aromatics), and PA (resins). Iso-octane was used as the reagent for separation. Subsequently, the maltene solution was treated by rotatory evaporation to remove the solvent. As can be seen, the viscosity of corn oil is the lowest, followed by commercial oil, and the viscosity of the maltenes is the highest.

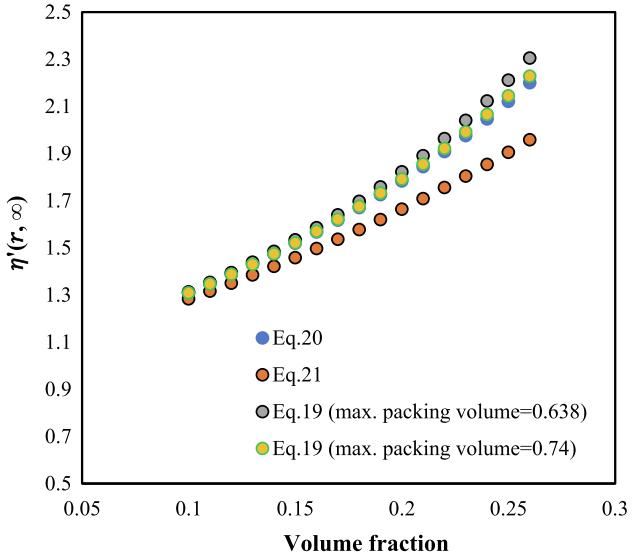

Fig. 4. Relationship between high-frequency viscosity with volume fraction.

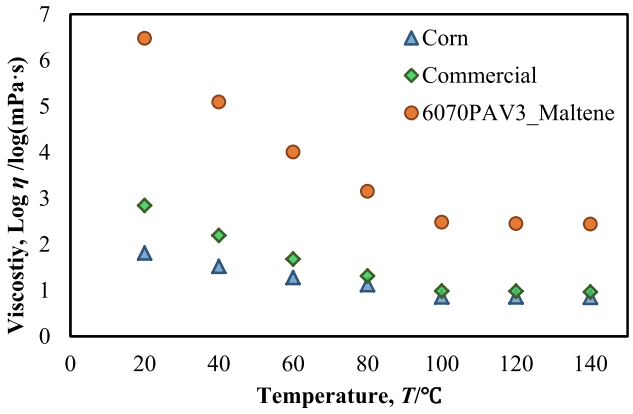

Fig. 5. Viscosity curves of the two rejuvenating agents and maltenes from 6070PAV3.

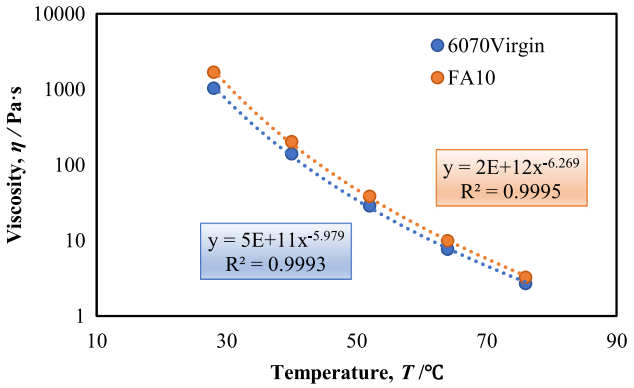

Fig. 6. Changes in maltene viscosity (binder 6070Virgin and FA10) with temperature.

The viscosities of the three fluids generally decrease with temperature, but at temperatures above 100 °C, no further dramatic decreases in viscosity can be found for all the fluids.

The weight and volume fractions of asphaltenes in asphalt binder samples are summarized in Table 2. In calculating the volume fractions, the density of asphaltenes is assumed to be 1.15 g/cm^3. Based on the previous measurements [9], the density of virgin or short-term aged asphalt binder is assumed to be 1.015 g/cm^3, and the density of long-term aged asphalt binder is 1.041 g/cm^3. For each of the two virgin asphalt binders, an increase in asphaltene content with aging can be observed. The laboratory-aged asphalt binder 80100PAV3 has the highest asphaltene content.

Changes in maltene viscosity with binder type and temperature are also shown in Table 2. Compared to the non-aged binders, the maltene viscosity of RTFO-aged binders increased at all temperatures. However, further aging does not necessarily increase maltene viscosity. Between 20 °C and 80 °C, the maltene viscosity can be well depicted as a power function. Two examples of the maltene viscosity versus temperature are shown in Fig. 6. The power equations are used to predict maltene viscosity at temperatures not tested.

The master curves of complex shear modulus and phase angle of all the samples were developed. Only asphalt binders 60/70, including those aged and rejuvenated, are shown for illustration purposes. In Fig. 7, the $|G^*|$ and δ values of different samples collapse together respectively at high frequencies (>10^5 rad/s). The highest value of $|G^*|$ reaches approximately 1 GPa, with δ approaching 0°. At the low-frequency end, δ approaches 90°, but the value of $|G^*|$ varies. Between low frequency and high frequency, a higher extent of aging is associated with higher $|G^*|$ and lower δ for a given value of ω_r, suggesting that the binders become stiffer and more elastic with aging.

The addition of both rejuvenators lowers the $|G^*|$ of the aged asphalt binder as well as increases its δ, as presented in Fig. 8. It is opposite to the trend as the asphalt binder ages. Therefore, using the two rejuvenators apparently "restore" the rheological properties of the asphalt binder. To a certain extent, the "rejuvenation" effect has been achieved. However, in the medium frequency range (10^{-3} to 10^3 rad/s), differences in δ between the aged and rejuvenated asphalt binders appear to be not as large as the differences in δ between the non-aged and aged binders.

3.2. The STEM images

Sample STEM images are provided in Figs. 9–12. Two typical nanoscale microstructures in darker color can be seen in all the images: a plate type made of random-packed nanoparticles and a needle (rod) type made of a well-ordered layered structure. Previous studies have indicated that such microstructures are asphaltenes [9,14]. Note that the brighter "bubble-like" features are the holes in the carbon films that support the samples.

The states of the microstructures appear to vary significantly with binder type, aging state, and rejuvenation. For asphalt binder Pen 80/100, microstructures are clearly visible in all three binders of different aging states. It also appears that the small particles tend to agglomerate to form large microstructures. Conversely, for asphalt binder Pen 60/70, visible microstructures in the non-aged binder are not abundant, although they still exist. Even though PAV aging for 60 hr significantly increases the asphaltene

Table 2
Asphaltene fraction and maltene viscosity of non-aged and aged asphalt binders.

Sample	Pen Grade (Before aging)	Aging treatment	Asphaltene fraction Weight g	Maltene Viscosity (Pa·s) Volume (cm^3)	76 °C	64 °C	52 °C	40 °C	28 °C
6070Virgin	60/70	None	0.20	0.18	2.70	7.70	28.85	140.44	1035.80
6070RTFO	60/70	RTFO	0.21	0.19	2.82	8.05	30.22	148.47	1118.89
6070PAV1	60/70	PAV, 20 hr	0.24	0.22	2.59	6.52	22.98	102.77	699.00
6070PAV3	60/70	PAV, 60 hr	0.26	0.23	2.77	7.80	28.62	138.06	1030.90
80100Virgin	80/100	None	0.22	0.19	1.52	4.01	12.58	49.08	265.09
80100RTFO	80/100	RTFO	0.23	0.20	2.32	6.47	22.79	109.77	775.56
80100PAV1	80/100	PAV, 20 hr	0.24	0.22	2.39	6.16	21.29	97.87	691.63
80100PAV3	80/100	PAV, 60 hr	0.28	0.25	1.94	5.16	17.86	82.54	578.70
FA5	60/70	Field, 5 yr	0.27	0.24	2.21	6.09	21.33	97.54	666.38
FA10	60/70	Field, 10 yr	0.29	0.26	3.27	9.98	38.56	203.75	1691.07

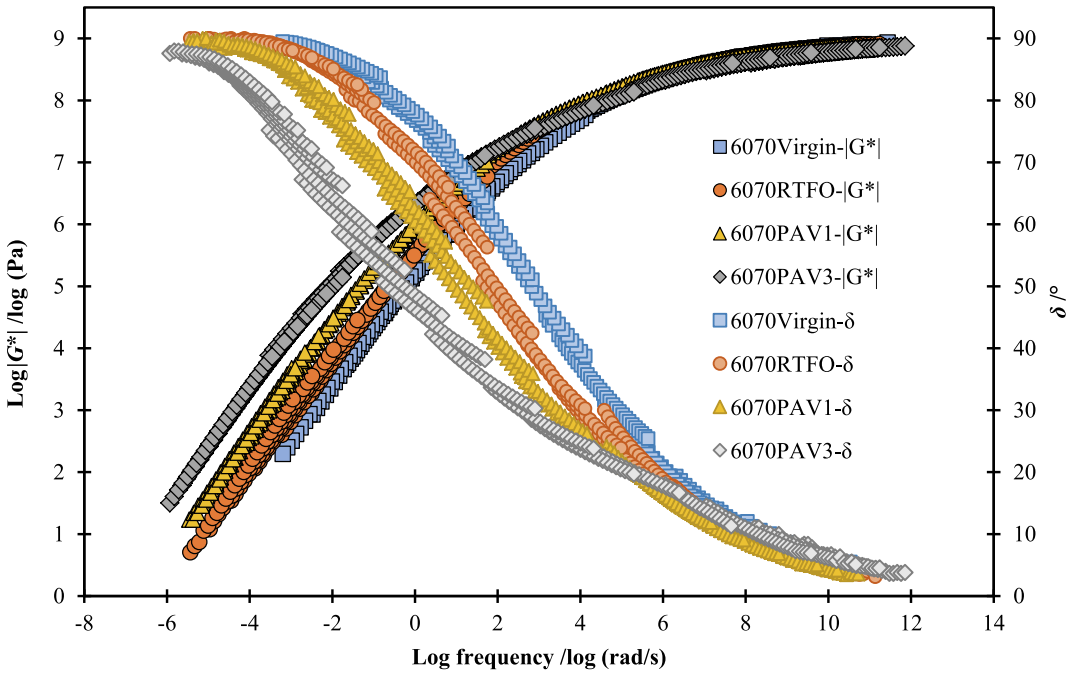

Fig. 7. Master curves of complex shear modulus and phase angle of the asphalt binder 60/70 at different aging states (Reference temperature: 25 °C).

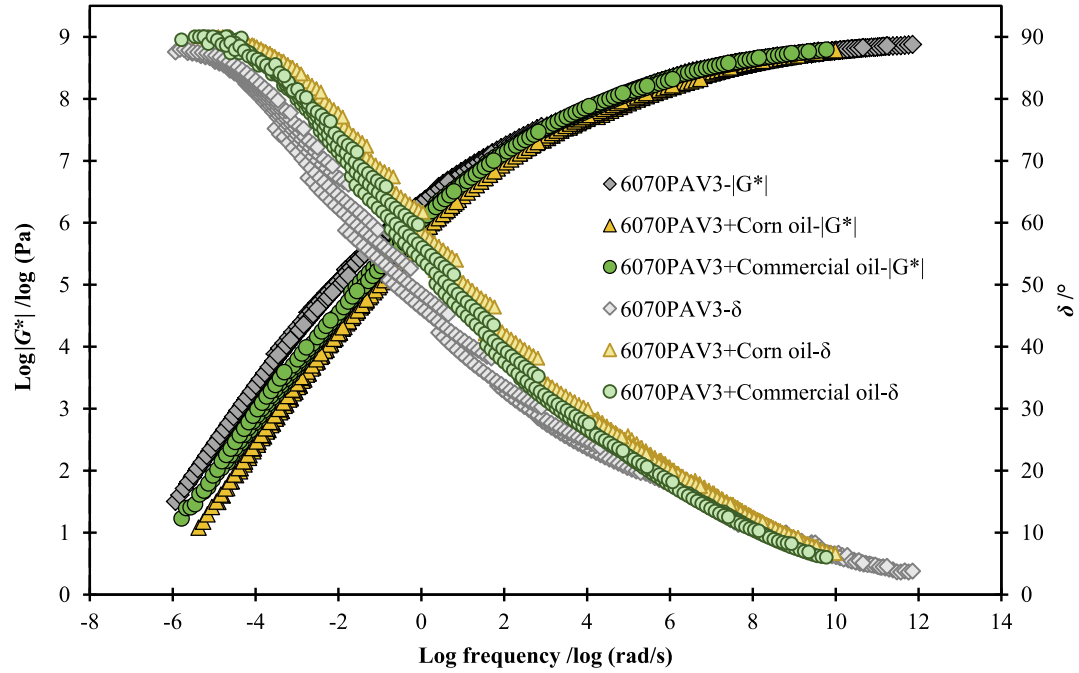

Fig. 8. Master curves of complex shear modulus and phase angle of the asphalt binder 60/70 subjected to triple PAV aging before and after rejuvenation (Reference temperature: 25 °C).

content in binder Pen 60/70 (Table 2), large asphaltene microstructures are not very common. This suggests that asphaltenes in the Pen 80/100 asphalt binder tested in this study are more likely to agglomerate than those in the Pen 60/70 binder tested in this study. However, this conclusion cannot be universally applied to all Pen 60/70 and Pen 80/100 asphalt binders.

Large microstructures are more abundant in field-aged asphalt binders (Fig. 11). In particular, rod-like microstructures can be easily seen in recovered binders from pavements of 10 years old. Similar plate-like and rod-like asphaltene microstructures have been reported in separated asphaltenes [14], solvent-deposited asphalt films [14], and solvent-free asphalt films [9,10]. At the same volume, changes in the aspect ratio of colloidal particles significantly affect the properties of the colloidal system, as extensively discussed in literature [11]. For instance, rotational relaxation is sensitive to the long dimension of the rod-like particles (Eq. (3)).

As shown in Fig. 12, the addition of the rejuvenators does not totally dissolve the associated asphaltene particles in any of the four combinations. However, rejuvenators still have some effects,

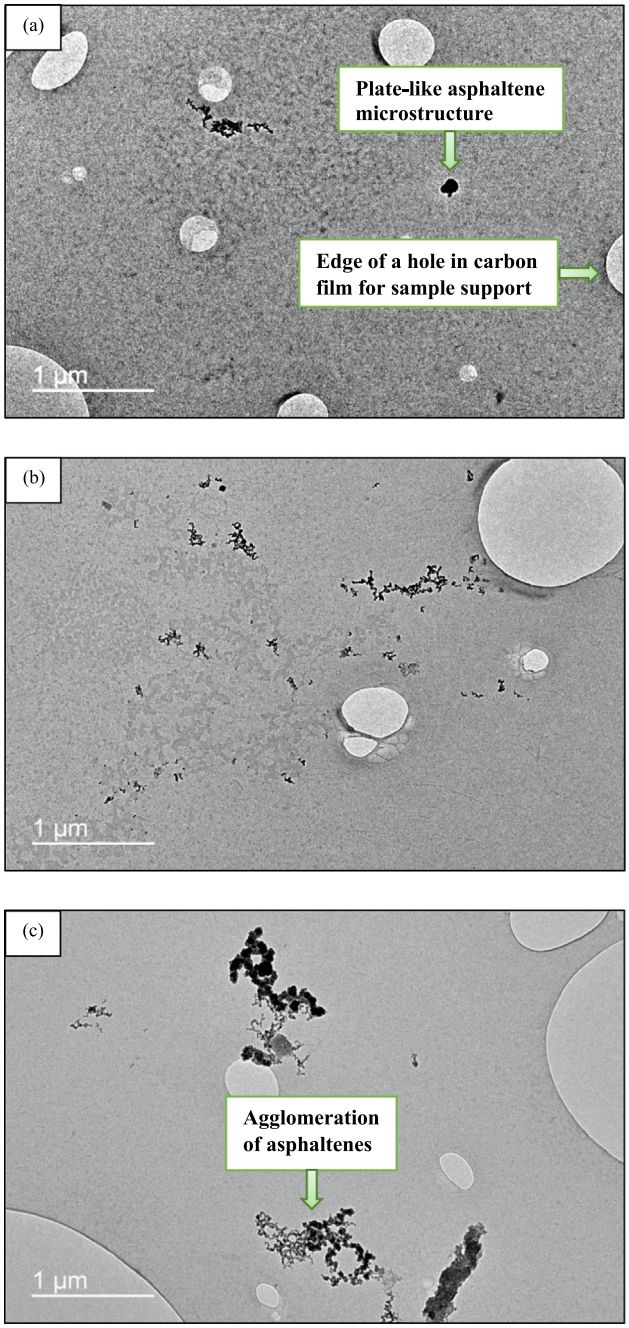

Fig. 9. STEM images of asphalt binder Pen 80/100 of different aging states: (a) 80100Virgin; (b) 80100RTFO; (c) 80100PAV3.

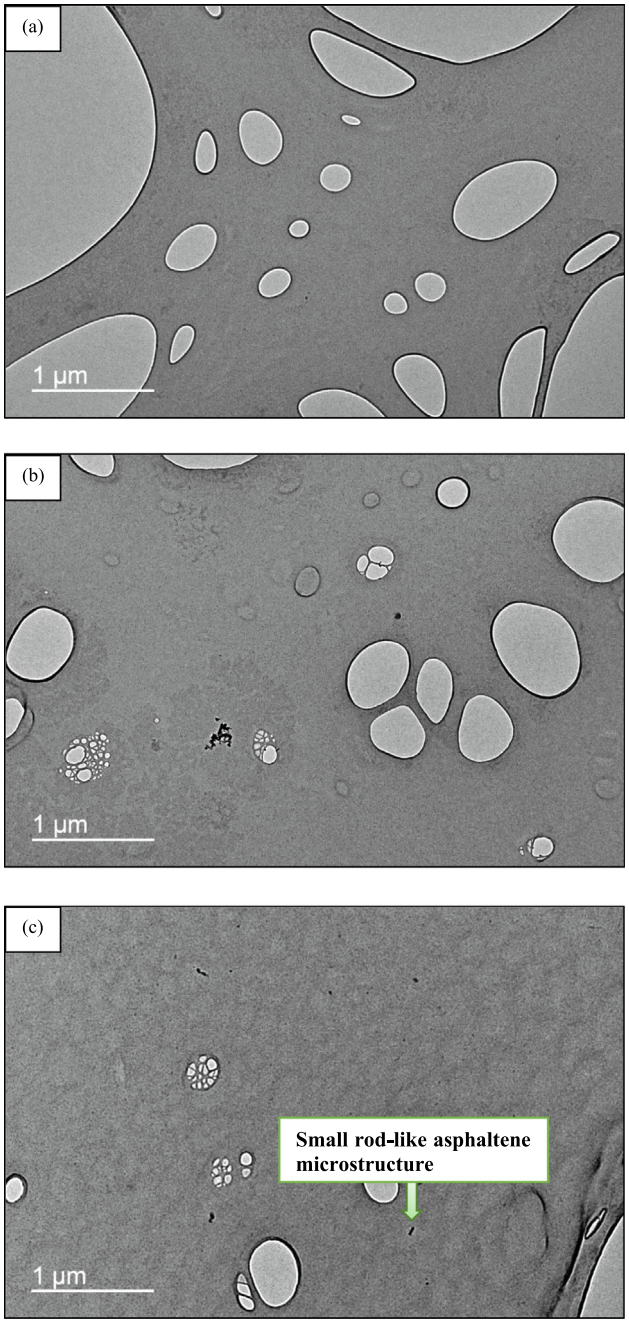

Fig. 10. STEM images of asphalt binder Pen 60/70 of different aging states: (a) 6070Virgin; (b) 6070RTFO; (c) 6070PAV3.

although the effects vary with binder type and rejuvenators. In rejuvenated FA5, large asphaltene microstructures are still widely available, and some rod-like microstructures are apparently intact. In rejuvenated FA10, however, there are apparent breakages of some large-size microstructures: Some rod-like microstructures are split, and small fragments of microstructures can be detected.

Moreover, circular features can be easily found in FA10 with commercial oil, yet this is uncommon in the original FA10. It provides evidence of interactions between rejuvenators and asphaltenes. Overall, these STEM images clearly reveal that the asphaltene microstructures vary between asphalt binders, and they evolve with aging and rejuvenation for the same type of asphalt binder.

3.3. The relaxation spectra and related parameters

3.3.1. The relaxation spectra

The impacts of microstructures shown in STEM images can hardly be quantified. In this section, the effects of microstructures are evaluated through relaxation spectra. The relaxation spectra of asphalt binders 60/70 and 80/100 at different states of aging and rejuvenation are shown in Figs. 13–16, respectively. The relaxation spectra of binders FA5 and FA10 are shown in Fig. 17 and Fig. 18, respectively. It can be observed that the obtained relaxation spectra are typically asymmetrical, bell-shaped curves with longer tails at the left side. The peak location, height, and width of those relaxation spectra apparently vary with the degree of aging and rejuvenation. However, a consistent trend is difficult to be found in

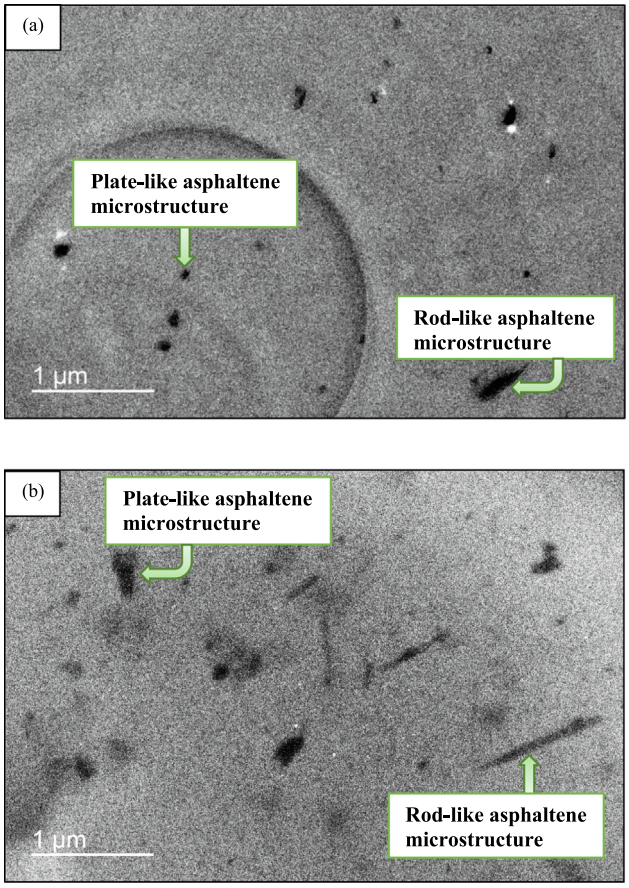

Fig. 11. STEM images of two field-aged asphalt binders: (a) FA5; (b) FA10.

relaxation spectra, except that aging extends the right tails of the relaxation spectra for the same asphalt binder while rejuvenation pushes the right tails back. Note that the right tail corresponds to longer relaxation time. The finding suggests that aging slows down the relaxation process while rejuvenation accelerates it. Specific changes in relaxation time at the right tails will be presented in later discussions. Note that changes in relaxation time with binder aging and rejuvenation are expected according to Eq. (17), Eq. (20), and Fig. 4.

3.3.2. The instantaneous shear modulus and glassy modulus

The instantaneous shear modulus $G(t=0)$ determined from relaxation spectra, and the glassy modulus G_g of asphalt binders at different states of aging and rejuvenation are provided in Table 3. For the same asphalt binder, the values of $G(t=0)$ and G_g are very close to each other. This partially validates the completeness of the relaxation spectra. In asphalt literature, G_g of asphalt binder is typically assumed to be 1 GPa. Values in Table 3 confirm that this is a reasonable assumption.

The values of $G(t=0)$ and G_g vary with aging and rejuvenation. In particular, RTFO aging apparently reduces these two values while PAV aging apparently increases them (as compared to the RTFO-aged binders). Rejuvenators significantly reduce $G(t=0)$ and G_g, often to a level less than that corresponding to the virgin binder. In addition, even though the viscosity of the commercial oil is higher than that of the corn oil at the tested temperature range, the $G(t=0)$ and G_g of binders rejuvenated by the commercial oil are comparably less.

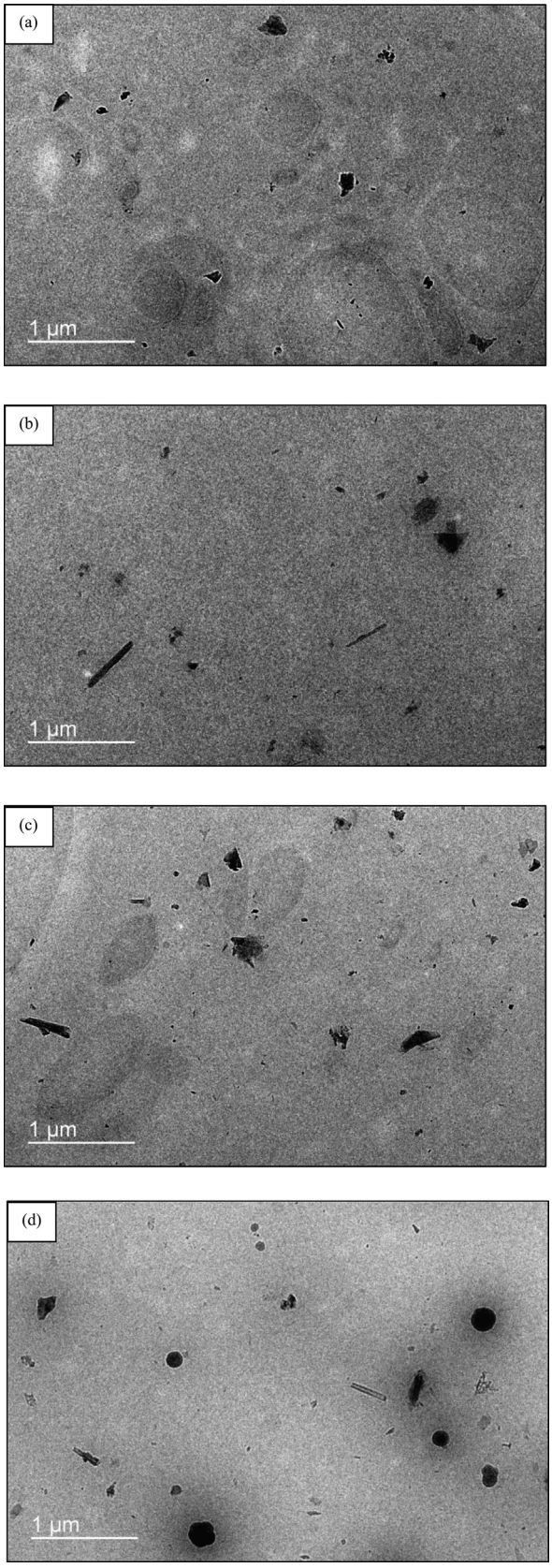

Fig. 12. STEM images of two rejuvenated asphalt binders: (a) FA5 added with corn oil; (b) FA5 added with commercial oil; (c) FA10 added with corn oil; (d) FA10 added with commercial oil.

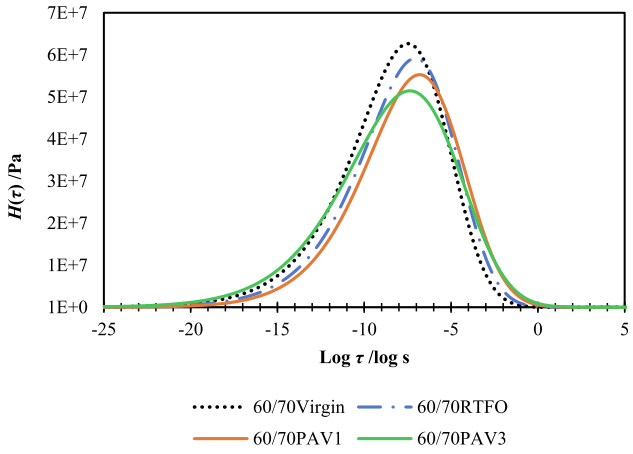

Fig. 13. Relaxation spectra of asphalt binder 60/70 at different levels of aging (Reference temperature: 25 °C).

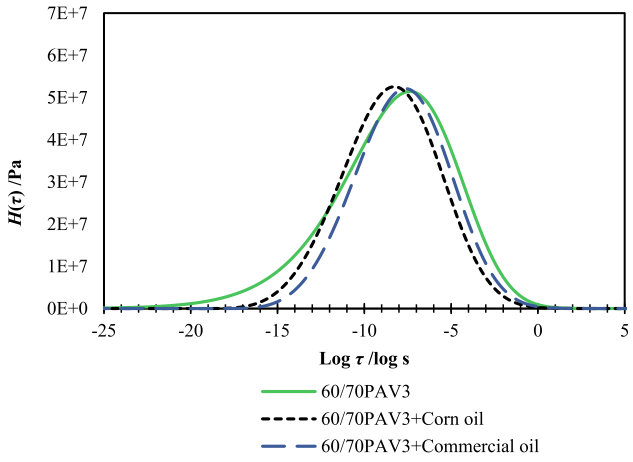

Fig. 14. Relaxation spectra of asphalt binder 60/70 subjected to triple PAV aging before and after rejuvenation (Reference temperature: 25 °C).

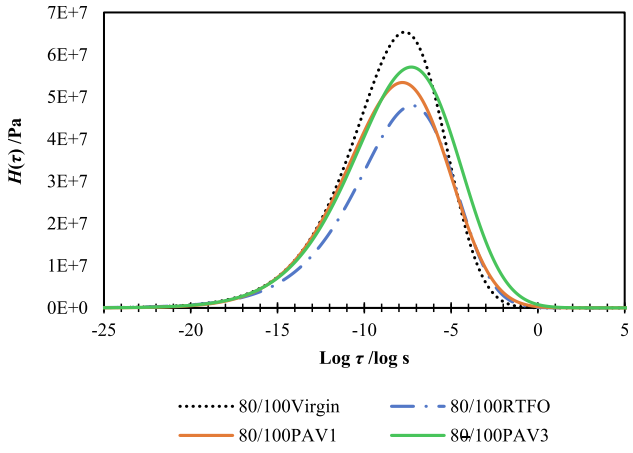

Fig. 15. Relaxation spectra of asphalt binder 80/100 at different levels of aging (Reference temperature: 25 °C).

3.3.3. The strength of relaxation corresponding to long relaxation time

The areas of relaxation spectra corresponding to long relaxation time (> 0.001 s) of asphalt binders at different levels of aging and rejuvenation are provided in Table 4. It can be observed that asphalt binders 6070Virgin and 80100Virgin had the lowest values

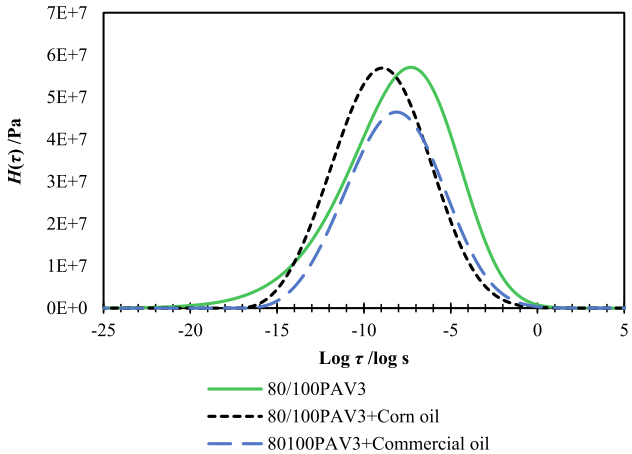

Fig. 16. Relaxation spectra of asphalt binder 80/100 subjected to triple PAV aging before and after rejuvenation (Reference temperature: 25 °C).

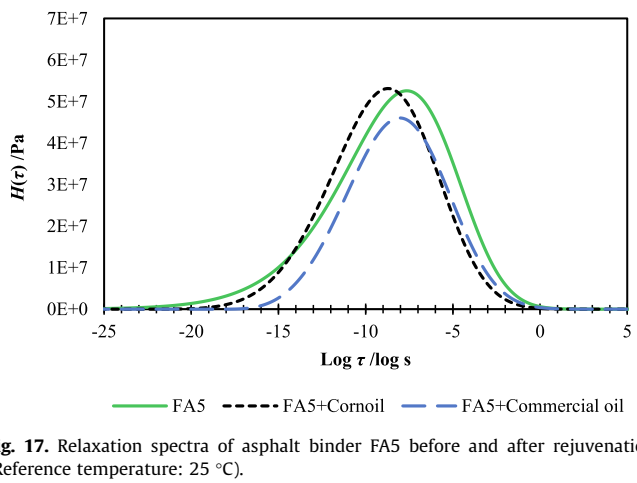

Fig. 17. Relaxation spectra of asphalt binder FA5 before and after rejuvenation (Reference temperature: 25 °C).

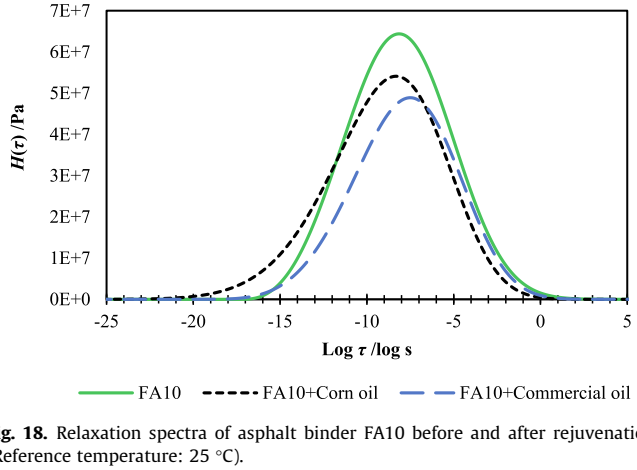

Fig. 18. Relaxation spectra of asphalt binder FA10 before and after rejuvenation (Reference temperature: 25 °C).

of $I_{H,\ LMS}$ at 1.12×10^7 and 0.89×10^7, respectively. The values of $I_{H,\ LMS}$ for both binders increased consistently after RTFO, one-time PAV aging, and triple-time PAV aging, but the rate of change differs with binder type. It appears that binder Pen 80/100 was more sensitive to aging than binder Pen 60/70 was. The values of $I_{H,\ LMS}$ for field-aged binders FA5 and FA10 were relatively higher than those of the 20-hour PAV-aged binders, but were comparable with those of the 60-hour PAV-aged binders. With the rejuvenation

Table 3
Instantaneous and glassy modulus at different levels of aging and rejuvenation of asphalt binders.

Parameter	Asphalt binder	Value of modulus (10^9 Pa)						
		Virgin	Aging				Rejuvenation	
			RTFO	PAV1	PAV3	Field	Corn	Commercial
$G(t=0)$ (1)	60/70	1.029	0.965	0.924	1.002	–	0.860	0.826
	80/100	1.037	0.813	0.936	1.034	–	0.908	0.744
	FA5	–	–	–	–	1.025	0.930	0.762
	FA10	–	–	–	–	1.137	1.028	0.850
G_g (2)	60/70	0.993	0.940	0.936	0.995	–	0.946	0.911
	80/100	1.020	0.787	0.919	0.982	–	0.904	0.841
	FA5	–	–	–	–	0.991	1.023	0.835
	FA10	–	–	–	–	1.158	1.081	0.950

(1) Obtained by Eq. (14).
(2) Obtained by regression of Black diagrams for $\delta = 0^{\circ}$ as explained in Section 2.3.2.

Table 4
The areas of the relaxation spectrum corresponding to long relaxation times.

Asphalt binder	$I_{H,\ \mathrm{LMS}}$ (10^7 Pa lns)						
	Virgin	Aging				Rejuvenation	
		RTFO	PAV1	PAV3	Field aging	Corn	Commercial
60/70	1.12	2.18	3.22	4.08	–	1.61	2.53
80/100	0.89	1.62	1.99	3.94	–	1.10	1.83
FA5	–	–	–	–	3.22	1.29	2.02
FA10	–	–	–	–	4.76	2.30	3.75

treatment of aged asphalt binders, $I_{H,\ \mathrm{LMS}}$ values significantly decreased. Compared with commercial oil, corn oil had a more pronounced effect, with more than half reduction in $I_{H,\ \mathrm{LMS}}$ for laboratory-aged and field-aged binders. In addition, a comparison of 6070PAV3, 80100PAV3, FA5, and FA10 binders treated by a same rejuvenating agent suggests that rejuvenation is the most effective for binder 80/100PAV3. The percent of $I_{H,\ \mathrm{LMS}}$ reduction for 80100PAV3 after being treated with corn oil and commercial oil was 27.9 % and 46.4 %, respectively. Overall, the relaxation strength at long relaxation time consistently depicts changes in relaxation behaviors of asphalt binders during aging and rejuvenation.

Changes in $I_{H,\ \mathrm{LMS}}$ during aging and rejuvenation are partially attributed to changes in asphaltene content during such processes. As suggested in Eq. (17), Eq. (20), and Fig. 4, an increase in asphaltene content will prolong the relaxation time or vice versa. Because aging causes increases in asphaltene content (Table 2) and the rejuvenators dilute the asphaltene content, changes in $I_{H,\ \mathrm{LMS}}$ during aging and rejuvenation are expectable. Another causes for changes in in $I_{H,\ \mathrm{LMS}}$ is attributed to changes in asphaltene particle size. As suggested in Eq. (17), the size effect is very significant as relaxation time is proportional to the cube of particle size. As revealed in the STEM images, the asphaltene particle size is generally increased after aging treatments, and there are some dissociations of asphaltene particles after rejuvenation. The agglomeration and dissociation of asphaltenes in aging and rejuvenation also caused the increase or decrease in $I_{H,\ \mathrm{LMS}}$ during the aging and rejuvenation process. The effects due to changes in asphaltene content or particle size may be separated, as shown in the following section.

3.3.4. The longest relaxation time and equivalent asphaltene particle size

The longest relaxation time of each asphalt binder is determined and shown in Table 5. Also shown in the table is the $\eta'_{r,\infty}$ and the equivalent asphaltene particle size (a_{eq}) as calculated according to Eq. (22). Similar to $I_{H,\ \mathrm{LMS}}$, the longest relaxation time is also consistent: Increases in aging are associated with obvious

Table 5
The areas of the relaxation spectrum corresponding to long relaxation times.

Sample	Longest Relaxation time,log(τ)	$\eta'_{r,\infty}$	Equivalent asphaltene particle size, a_{eq}
6070Virgin	3.29	1.66	112.92
6070RTFO	3.90	1.72	172.03
6070PAV1	4.78	1.89	393.68
6070PAV3	6.19	2.00	986.90
6070PAV3 + Corn oil	4.69	1.95	445.49
6070PAV3 + Commercial oil	4.88	1.96	461.86
80100Virgin	3.08	1.74	151.97
80100RTFO	3.96	1.78	203.68
80100PAV1	4.78	1.88	396.48
80100PAV3	6.03	2.15	1040.91
80100PAV3 + Corn oil	5.18	2.05	760.95
80100PAV3 + Commercial oil	5.41	2.06	822.70
FA5	5.44	2.08	631.47
FA5 + Corn oil	4.94	1.98	607.66
FA5 + Commercial oil	5.12	1.99	631.97
FA10	8.21	2.22	2985.90
FA10 + Corn oil	4.81	2.11	409.86
FA10 + Commercial oil	5.57	2.11	655.50

increases in the longest relaxation time, and rejuvenators reduce the longest relaxation time. Aging and rejuvenation can cause a significant (often more than ten times) difference in the longest relaxation time. Therefore, the longest relaxation time is quite sensitive to the underlying physicochemical changes of asphalt binders during aging and rejuvenation. Compared with commercial oil, corn oil is slightly more effective in reducing the longest relaxation time.

As shown in Eq. (17), the longest relaxation time is determined by both the high-shear limit viscosity of the asphalt binder and asphaltene morphology. It is proposed in this study to use the equivalent asphaltene particle size a_{eq} to represent the size effect of asphaltenes (Eq. (22)). The last column of Table 5 indicates

changes in a_{eq} during aging and rejuvenation. To a certain extent, the parameter a_{eq} excludes (or at least reduces) the influences of maltene viscosity and asphaltene content. It can be seen that, for the same asphalt binder, a_{eq} increases with binder aging. The largest a_{eq} is seen in binder FA10, in which a large number of rod-like asphaltene particles can be found in the STEM images. Evidently, the asphaltene size effect is reflected in a_{eq}. Rejuvenators can generally reduce the a_{eq}, except for FA5 rejuvenated with the commercial oil, implying that the commercial oil at the chosen dosage (4.5 %) may be less effective. STEM images (Fig. 12) also indicate that the two rejuvenators apparently do not break down the large-size asphaltene microstructures in FA5 as effectively as they did in FA10. Table 5 also revealed that a_{eq} of the rejuvenated asphalt binder by corn oil is consistently smaller than a_{eq} of the rejuvenated binder by commercial oil. Therefore, a_{eq} can offer some interesting and useful insights not given by the $I_{H,\ LMS}$ and the longest relaxation time.

4. Summary and conclusion

The engineering property changes of asphalt binder during aging and rejuvenation are governed by its fundamental physicochemical property transitions. Using binders from different sources and of different aging/rejuvenation states, this study investigated the relaxation spectra of the asphalt binders and the connections between relaxation spectra and the characteristics of asphaltenes and maltenes. A meticulous effort was made to build complete and reliable relaxation spectra. Asphaltenes and maltenes in each binder were separated and analyzed in detail. Asphaltenes in aged and rejuvenated asphalt binders were also examined by using STEM. Connections were established between the relaxation spectra and characteristics of asphaltenes and maltenes, with STEM images serving as additional and direct pieces of evidence. The following major conclusions can be drawn from the study:

(1) The strength of relaxation spectra corresponding to long relaxation time (e.g., $\log(\tau) > -3$) or the longest relaxation time of the asphalt binder well captures its fundamental physicochemical property changes in aging and rejuvenation.
(2) The strength of relaxation spectra corresponding to long relaxation time or the longest relaxation time of the asphalt binder is sensitive to the morphological changes of asphaltene microstructures.
(3) Agglomerated asphaltene microstructures after rejuvenation are not totally dissolved, but changes in morphology can be detected.
(4) Changes in asphaltene microstructures after rejuvenation are affected by asphalt binder type and rejuvenator type.
(5) The newly developed indicator—equivalent asphaltene particle size (a_{eq})—provides a theoretically sound parameter to understand what occurs at the nanoscale in asphalt binder aging and rejuvenation.

CRediT authorship contribution statement

Fangjin Li: Writing – original draft. **Yuhong Wang:** Conceptualization, Writing – review & editing. **Miomir Miljković:** Writing – review & editing. **Kin Ming Chan:** .

Declaration of Competing Interest

The authors declare that they have no known competing financial interests or personal relationships that could have appeared to influence the work reported in this paper.

Acknowledgment

The article is based on the research project (Project Number: PolyU 152568/16E; 15213020) funded by the Research Grants Council of the Hong Kong Special Administrative Region Government.

References

[1] L.W. Corbett, Composition of asphalt based on generic fractionation, using solvent deasphaltening, elution-adsorption chromatography, and densimetric characterization, Anal. Chem. 41 (4) (1969) 576–579, https://doi.org/10.1021/ac60273a004.
[2] J.C. Petersen, A review of the fundamentals of asphalt oxidation: chemical, physicochemical, physical property, and durability relationships, Transp. Res. Circular (2009) (E-C140).
[3] J. Wang, T. Wang, X. Hou, F. Xiao, Modelling of rheological and chemical properties of asphalt binder considering SARA fraction, Fuel 238 (2019) 320–330, https://doi.org/10.1016/j.fuel.2018.10.126.
[4] C. Mack, Colloid chemistry of asphalts, J. Phys. Chem. 36 (12) (1932) 2901–2914.
[5] K.L. Gawrys, P. Matthew Spiecker, P.K. Kilpatrick, The role of asphaltene solubility and chemical composition on asphaltene aggregation, Pet. Sci. Technol. 21 (3–4) (2003) 461–489, https://doi.org/10.1081/LFT-120018533.
[6] D. Lesueur, The colloidal structure of bitumen: Consequences on the rheology and on the mechanisms of bitumen modification, Adv. Colloid Interface Sci. 145 (1–2) (2009) 42–82, https://doi.org/10.1016/j.cis.2008.08.011.
[7] R.N. Hunter, A. Self, J. Read, E. Hobson, The shell bitumen handbook, Ice Publishing, London, UK, 2015, p. 789.
[8] M. Liu, J.M. Chaffin, R.R. Davison, C.J. Glover, J.A. Bullin, Changes in Corbett fraction composition during oxidation of asphalt fractions, Transp. Res. Rec. 1638 (1) (1998) 40–46, https://doi.org/10.3141/1638-05.
[9] Y. Wang, K. Zhao, F. Li, Q. Gao, K.W.C. Lai, Recent advances in characterizing the "bee" structures and asphaltene particles in asphalt binders, Int. J. Pavement Res. Technol. 13 (6) (2020) 697–706, https://doi.org/10.1007/s42947-020-6008-3.
[10] Y. Wang, K. Zhao, F. Li, Q.i. Gao, K.W.C. Lai, Asphaltenes in asphalt: Direct observation and evaluation of their impacts on asphalt properties, Constr. Build. Mater. 271 (2021) 121862, https://doi.org/10.1016/j.conbuildmat.2020.121862.
[11] J. Mewis, N.J. Wagner, Colloidal suspension rheology, Cambridge University Press, 2012.
[12] O.C. Mullins, H. Sabbah, J. Eyssautier, A.E. Pomerantz, L. Barré, A.B. Andrews, Y. Ruiz-Morales, F. Mostowfi, R. McFarlane, L. Goual, R. Lepkowicz, T. Cooper, J. Orbulescu, R.M. Leblanc, J. Edwards, R.N. Zare, Advances in asphaltene science and the Yen-Mullins model, Energy Fuels 26 (7) (2012) 3986–4003.
[13] S. Fakher, M. Ahdaya, M. Elturki, A. Imqam, Critical review of asphaltene properties and factors impacting its stability in crude oil, J. Pet. Explor. Prod. Technol. 10 (3) (2020) 1183–1200.
[14] Y. Wang, K. Zhao, Different forms of asphaltene microstructures discovered in transmission electron microscopy, J. Mater. Civ. Eng. 28 (11) (2016) 04016137, https://doi.org/10.1061/(ASCE)MT.1943-5533.0001660.
[15] A. Koyun, J. Büchner, M.P. Wistuba, H. Grothe, Rheological, spectroscopic and microscopic assessment of asphalt binder ageing, Road Mater. Pavement Des. 23 (1) (2022) 80–97, https://doi.org/10.1080/14680629.2020.1820891.
[16] D. Yu, Y. Gu, X. Yu, Rheological-microstructural evaluations of the short and long-term aged asphalt binders through relaxation spectra determination, Fuel 265 (2020) 116953, https://doi.org/10.1016/j.fuel.2019.116953.
[17] F. Li, Y. Wang, K. Zhao, The hierarchical structure of bitumen of different aging states at the molecular level and nanoscale, Fuel 319 (2022) 123791, https://doi.org/10.1016/j.fuel.2022.123791.
[18] M. Doi, Diffusion-controlled reaction of polymers, Chem. Phys. 9 (3) (1975) 455–466, https://doi.org/10.1016/0301-0104(75)80083-8.
[19] T. Shikata, D.S. Pearson, Viscoelastic behavior of concentrated spherical suspensions, J. Rheol. 38 (3) (1994) 601–616, https://doi.org/10.1122/1.550477.
[20] T. Zhou, L. Cao, E.H. Fini, L. Li, Z. Liu, Z. Dong, Behaviors of asphalt under certain aging levels and effects of rejuvenation, Constr. Build. Mater. 249 (2020) 118748, https://doi.org/10.1016/j.conbuildmat.2020.118748.
[21] K. Zhao, Y. Wang, L. Chen, F. Li, Diluting or dissolving? The use of relaxation spectrum to assess rejuvenation effects in asphalt recycling, Constr. Build. Mater. 188 (2018) 143–152, https://doi.org/10.1016/j.conbuildmat.2018.08.098.
[22] B. Zhmud, Viscosity blending equations, Lube Mag 121 (2014) 2–5.
[23] K. Chan, Y. Wang, Determination of the master curves of shear modulus and phase angle for asphalt binders with consideration of relaxation spectrum, Int. J. Pavement Eng. 1–15 (2021), https://doi.org/10.1080/10298436.2021.1907578.
[24] M.T. Shaw, W.J. MacKnight, Introduction to polymer viscoelasticity, John Wiley & Sons, 2018.
[25] V. Kontogiorgos, Calculation of relaxation spectra from mechanical spectra in MATLAB, Polym. Test. 29 (8) (2010) 1021–1025, https://doi.org/10.1016/j.polymertesting.2010.09.007.

[26] N.I.M. Yusoff, E. Chailleux, G.D. Airey, A comparative study of the influence of shift factor equations on master curve construction, Int. J. Pavement Res. Technol. 4 (6) (2011) 324.
[27] L.N. Mohammad, Z. Wu, L. Myers, S. Cooper, C. Abadie, A practical look at the simple performance tests: Louisiana's experience (with discussion), J. Assoc. Asphalt Paving Technol. 74 (2005).
[28] H.W. Bode, Relations between attenuation and phase in feedback amplifier design, Bell Syst. Tech. J. 19 (3) (1940) 421–454, https://doi.org/10.1002/j.1538-7305.1940.tb00839.x.
[29] H.C. Booij, G.P.J.M. Thoone, Generalization of Kramers-Kronig transforms and some approximations of relations between viscoelastic quantities, Rheol. Acta 21 (1) (1982) 15–24.
[30] R.D.L. Kronig, On the theory of dispersion of x-rays, Josa 12 (6) (1926) 547–557.
[31] R.M. Fuoss, J.G. Kirkwood, Electrical properties of solids. VIII. Dipole moments in polyvinyl chloride-diphenyl systems, J. Am. Chem. Soc. 63 (2) (1941) 385–394.
[32] D.A. Anderson, D.W. Christensen, H.U. Bahia, R. Dongre, M.G. Sharma, C.E. Antle, J. Button, Binder characterization and evaluation: Physical characterization, vol. 3, Strategic Highway Research Program, National Research Council, Washington, DC, 1994.
[33] I.M. Krieger, T.J. Dougherty, A mechanism for non-Newtonian flow in suspensions of rigid spheres, Trans. Soc. Rheol. 3 (1) (1959) 137–152, https://doi.org/10.1122/1.548848.
[34] R.A. Lionberger, W.B. Russel, Microscopic theories of the rheology of stable colloidal dispersions, Adv. Chem. Phys. 111 (2000) 399–474.
[35] A.J. Banchio, G. Nägele, Short-time transport properties in dense suspensions: from neutral to charge-stabilized colloidal spheres, J. Chem. Phys. 128 (10) (2008) 104903, https://doi.org/10.1063/1.2868773.